Student
Louison Thorens
M2 - Physique, concepts et applications
École Normale Supérieure de Lyon
louison.thorens[at]ens-lyon.fr
(+33)6 15 31 24 37

Supervisor
Mickaël Bourgoin
Laboratoire de Physique
École Normale Supérieure de Lyon
mickael.bourgoin[at]ens-lyon.fr
(+33)4 26 23 39 54

Internship report

Ferromagnetic beads sedimentation forced by an external magnetic field

Abstract

This document reports the work I did under the supervision of Mickaël Bourgoin and Valérie Vidal at the Laboratoire de Physique at the ENS de Lyon. The topic deals with the sedimentation of ferromagnetic beads inside a Hele-Shaw cell under the forcing of an external magnetic field. The interactions between the beads play a key role in the mechanism of sedimentation through the formation of clusters. We propose here a granular-type analysis followed by a dynamic approach. Finally, some basic elements of comprehension are missing, that is why we also propose two studies needed and planned in our future work. This subject is very promising, and leads us to a full variety of problems and analysis, this report paves the way towards to a more complete study in the near future.

Aknowledgments

I would like to thank Mickaël for welcoming me in the past few months and for leading me on this promising subject. I would also like to thank Valérie Vidal for her expertize in granular media that led me to a better comprehension of my experiment. I also had the opportunity to work during a few weeks with Filippo Coletti from the University of Minnesota on the hydrodynamic issues of sedimentation inside a Hele-Shaw cell. Finally, a thanks to Jérémy Vessaire for lighting me with his knowledge on suspension mechanics, and for helping me build the experimental setup.

Contents

Introduction

Particle laden flows are quite common in the industry or in nature, such as geophysical flows of volcanos. These flows are generally turbulent and it is therefore quite complicated to fully describe the different effects at play, such as the interactions of the particles with the flow, with the environnement and also between particles. Because of this large variety of mechanisms there is, at the moment, no general satisfactory equation to describe the transport of particules in flows. One of the major issues when studying these flows is the fact that the mass of a particle in turbulent suspension intervenes both in intertia and gravity. Our proposition is to separate the two aspects of the mass by controling the effective gravitational mass. To do so we propose to impose an external magnetic field on magnetic particles in order to counteract the gravitationnal force. Besides, when many particles are present, the induced magnetization results in additionnal particle/particle interactions which can be of interest to model realistic natural and industrial particle laden flows where electrostatic and magnetic interactions can exist.
The present study constitutes a first step towards this mid-term goal and aims at carrying some preliminary investigations of magnetic laden flows in simplified configurations. We chose to use ferromagnetic beads since their magnetic susceptibility is high and the effects are clearer. We start by studying a quasi-2D suspension of beads inside a Hele-Shaw cell to apprehend some of the phenomena involved. This experiment, quite basic, reveals a large amount of phenomena with a panel of applications in industry [1] [2], in granular physics [3] [4], in biology [5] and also in medicine [6].
Since our experiment is very promising and seems to abound with research topics, we propose in this report to expose the different studies we performed. We started by a granular analysis of the structure obtained when the beads sediment under the influence of a homogeneous external magnetic field. Because of the various zoology of structures obtained, we have then focused on the dynamics of sedimentation with tuned interactions between the beads, and study the sedimentation of beads clusters. Finally, we propose in this report some thoughts on future works that need to be done to fully apprehend the total mechanisms of ferromagnetic beads sedimentation under a magnetic field.

I Generalities

1 Experimental setup

In order to study the case of ferromagnetic beads sedimentation under an external magnetic field, we decided to study in a first approach the quasi-2D case. To do so we used as a container, a Hele-Shaw cell, *i.e.* two parallel walls separated by a small gap, in our case the gap is 750 µm. The cell can be flipped back and forth to investigate the settling properties of the particles. Since our particles are steel beads 500 µm diameter (appendix A), we have a mono-layer of beads inside the cell. The cell is filled with a water-glycerol mixture, in our case 77% of mass in glycerol, leading to a viscosity $\mu = 44.53\,10^{-3}$ Pa · s. Finally, the density of our beads is measured to be $\rho = 8.2\,10^3$ g · m^{-3}, leading to a Reynolds number in our case of $Re = \frac{\rho d v_s}{\mu} \approx 1$, with v_s the typical settling velocity, of the order of 10^{-2}.

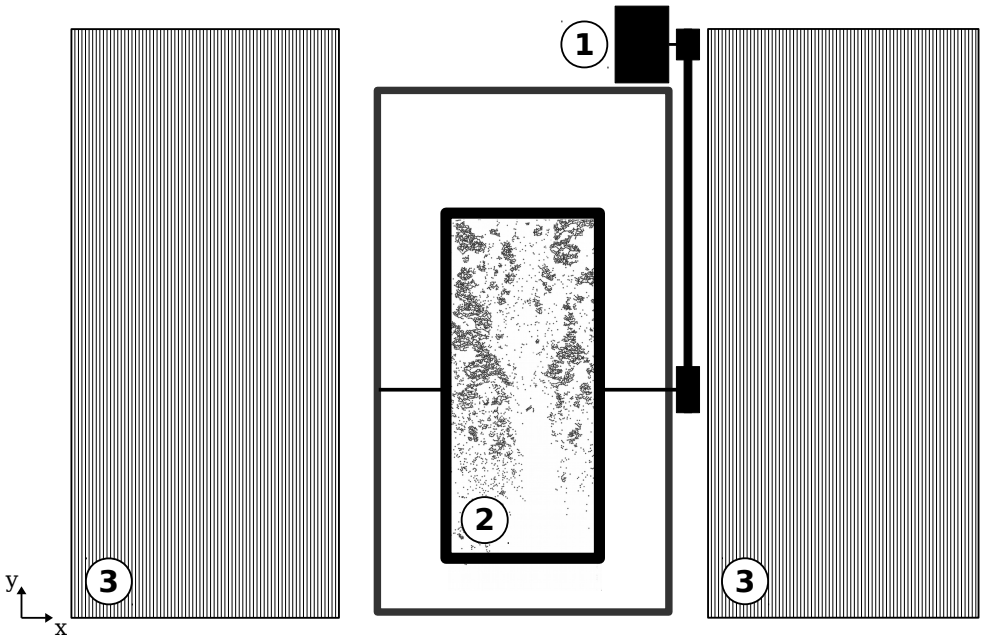

Figure 1: The experimental setup. — **1** : stepper motor controled via a Raspberry Pi card — **2** : Hele-Shaw cell containing the water-glycerol mixture and the ferromagnetic beads — **3** : Helmoltz coils.

Now that we have presented our experimental setup, we will briefly present the protocol. In order to perform statistically converged results, we fully automatised the experimental setup through a Raspberry Pi card driving the magnetic field generator, the reversing motor and the camera.
The protocol is quite simple and is divided in three phases:

1. sedimentation when we flip the cell and wait for the full sedimentation of the beads, fig. (2b,2c),

2. final structure when we wait for the stabilisation of the final and sedimented structure at the bottom of the cell, fig. (2d),

3. reboot when we flip again the cell to return in the original situation, during this reboot sedimentation we also perform a demagnetisation of the beads as explained in the next section, fig. (2a).

The data is obtained during the "sedimentation" and the "final structure" phases depending on the interest. This is the classical protocol used for the majority of the results presented in this report. The

(a) (b) $t = 0$ (c) (d) t_{final}

Figure 2: Different phases of the experimental protocol.

final section will present a slightly different protocol, for the study of "homogeneous sedimentation".

2 Ferromagnetic materials

The beads that we used are made of steel, known to be a ferromagnetic material. Such material is characterized by a high positive value of its magnetic susceptibility χ, *i.e.* its magnetic response to an external magnetic field. In our case the susceptibility has been measured to be $\chi = 44$, appendix B. When a magnetic field $\vec{H}$ is applied, each bead becomes an induced magnetic dipole with magnetization $\vec{m} = \chi V \vec{H}$, with V the volume of a bead. Therefore, we can easily tune the interactions between beads by tuning the magnetic field created by our Helmoltz coils.
One drawback of this type of material is the existence of a remanent magnetization B_r. Without any external magnetic field, each bead possesses an intrisic magnetization created by its past forcing. This remanent field has to be supressed between each measurement to be sure that experiments are done in the same conditions: it is the demagnetization process. Fig. (3) represents the typical hysteresis of magnetization of a ferromagnetic material in blue, the remanent field is noted B_r. There are two possible ways to demagnetize the material; firstly one can apply the coercive field H_c as the external magnetic field but it has to be known, secondly one can follow the "demagnetization path", in red, to progressively decrease B_r until reaching zero, this is the most common solution. In practice, we apply an oscillating forcing field with a continuously decreasing amplitude.

Finally, we briefly present the magnetic interaction between the beads inside our Hele-Shaw cell. In general, we consider two magnetic spheres (i and j), represented by two magnetic dipoles: m_i and m_j. The distance between these two spheres is noted r_{ij}. The interaction energy is given by [8] and writes as:

$$U_{ij} = \frac{1}{4\pi\mu_0}\left[\frac{\vec{m}_i \cdot \vec{m}_j}{r_{ij}^3} - 3\frac{(\vec{m}_i \cdot \vec{r_{ij}})(\vec{m}_j \cdot \vec{r_{ij}})}{r_{ij}^5}\right] \tag{1}$$

In our particular case, presented in fig. (4), the two momenta are equal to $\chi V \vec{H} = \chi V \frac{\vec{B}}{\mu_0}$ for ferromagnetic materials, with χ the magnetic susceptibility, $\vec{B} = B_0 \vec{x}$ the external magnetic field

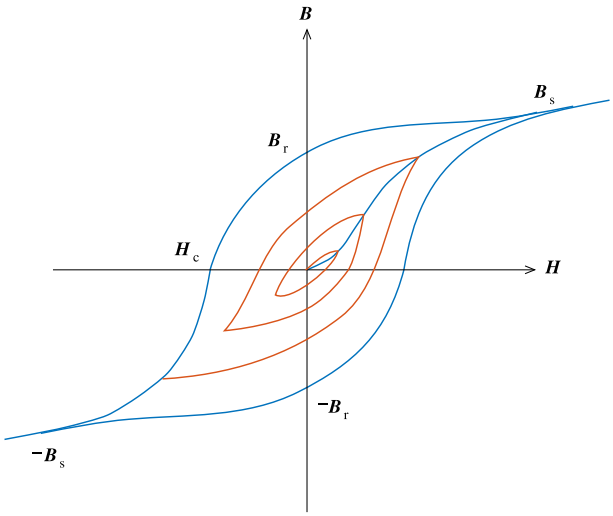

Figure 3: Hysteresis, in blue, of magnetization for a ferromagnetic material, taken from [7]. The remanent field is noted B_r, the coercive field H_c and the saturation field B_s. The demagnetization path is represented in red.

(uniform and horizontal) and V the volume of a sphere. If we note a the radius of a sphere, then the interaction energy simplifies as:

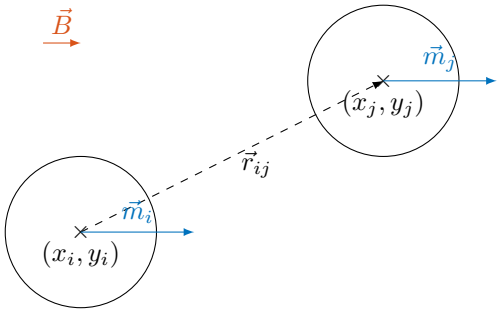

Figure 4: Interaction bewteen two beads in our particular case.

$$U_{ij} = \frac{\mu_0}{4\pi}\left(\frac{4}{3}\pi a^3 \chi B0\right)^2 \left[\frac{1}{r_{ij}^3} - 3\frac{(x_j - x_i)^2}{r_{ij}^5}\right] \tag{2}$$

3 Voronoï diagram

We introduce in this section a tool largely used in suspension physics, Voronoï tessalation. The typical representation of such a diagram is given in fig. (5b).
A Voronoï diagram is an assembly of regions generated by a set of generating seeds. Each point inside the region generated by a seed is closer to that seed than any other. If applied to the spatial distribution of the particles, we can interprete the Voronoï diagram as the plot of influence regions associated to each bead.
An example of the generation of such a diagram is given in fig. (5). In this example the set of generating seeds is given by a random distribution of 200 points. Different algorithms can be used to compute the Voronoï diagram of any set of points. These techniques such as the "perpendicular bisector method" and the Avrami–Johnson–Mehl method are presented in reference [9]. Once the

diagam is computed, we "clean" it since the borders of this diagram are biased by the finite size of the domain of interest and do not represent any physical constraint. Finally, the area of each Voronoï cell is computed and plotted in the final diagram, fig. (5c), from blue for the smallest areas to yellow for the larger ones

Many basic information can be derived through the distribution of the Voronoï areas such as the compactness discussed in the next section. The Voronoï diagram can also be used to perform Particle Tracking Velocimetry (PTV), as it is presented in [10] and [11], what is a perspective of this work.

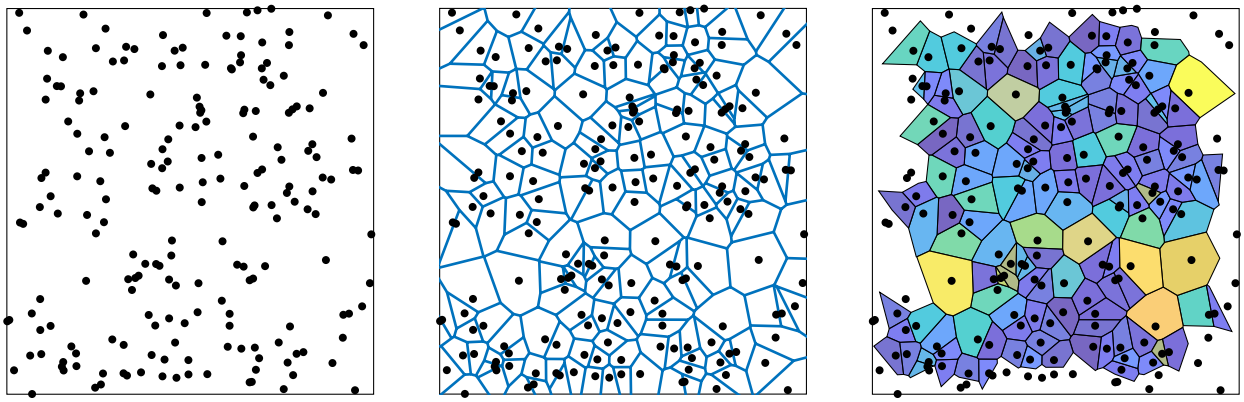

(a) Random generation of 200 points. (b) Voronoï diagram. (c) Areas of the Voronoï diagram.

Figure 5: We generated a set of 200 points and then computed their Voronoï diagram. Because the border regions are not physical, we clean the Voronoï diagram and compute the areas of the Voronoï regions: the colorbar starts from blue for the smallest areas to yellow for the biggest areas.

II Granular analysis

1 Static study: final structure

The first study that we have performed on our sedimenting beads is the analysis of the final sedimented structure, fig. (2d). This final system is a steady mono-layer of grains which nature depends only on the interaction between beads, *i.e.* the forcing field value. The final structure extends over a wide range of shapes, presented in appendix C.
Since the final system is composed of steady stacked beads we start by analysing some typical granular physics parameters.

Compactness. The first quantity that we decided to compute is the compactness of the final sedimented structure made by all the beads. The compactness is a classical granular quantity defined as follows:

$$C = \frac{area_{beads}}{area_{filled}} = \frac{area_{beads}}{area_{beads} + area_{holes}} \left(= \frac{px_{beads}}{px_{filled}} \right) = \frac{N \times \pi a^2}{area_{filled}}, \tag{3}$$

with px_{beads} the number of pixels filled by the beads, px_{filled} the number of pixels filled by the beads and the holes, N the number of beads, a the radius of one bead. A simple representation of the different regions inside the final structure may be found in fig. (7a).
The definition of the compactness is here adapted to our quasi-2D experiment, we will work only with the apparent areas. The first approach that we used to compute the compactness was to compare the number of pixels of the beads and of the filled image (holes+beads). Unfortunately, one has to be careful when using this definition since the number of pixels attributed to each bead may vary when changing the topology (issues mainly due to the illumination). The number of pixels assigned to each bead decreases with the external field (since the structure is less compact and the luminosity varies), as it is shown in the following table:

Field (mT)	0.0	0.55	1.10	1.65	2.0	2.56	3.11
$area_{bead}$	37.9	37.9	37.8	37.5	37.1	36.8	36.5

Therefore, we decided to use the final definition of the compactness using the real projected area of each bead (πa^2) and the number N of detected particles. The beads are detected according to their centers since it is a local minimum of intensity.
The resulting plot for the compactness is plotted in blue in fig. (6). Firstly, and this will be the case in all of our results in this section, there is a maximum limit for the external field imposed by the geometry of our cell. In fact, for an external field above 3.66 mT the structure of beads does not sediment and stays on the top of the cell. We have two different explanations for this experimental limit:

- the structure is so solid that the fluid cannot percolate between the beads and therefore the beads structure cannot fell inside the cell,
- the structure touches the borders of the cell and is so solid that the chain forces are greater than its weight and therefore it cannot fell.

We therefore limit our study at amplitudes of applied magnetic field below 3.66 mT. We first note that the values for the compactness are in agreement with the maximum limit (≈ 0.9 for a full compact packing) and with the value of 0.82 obtained in numerical simulations [12]) for 2D random close packing. Our results are a bit below this simulated value where the apparation of a new bead is random while in our case there is a privileged direction.
The first direct observation on the compactness of the final structure is that it decreases as the forcing field increases, *i.e.* the stronger the interaction between the beads, the looser the final structure; what

may seem counter-intuitive at first sight, as particle/particle interactions are stronger as the applied field increases. To understand this phenomenon, we have to embrace quickly what is going on when a forcing field is applied. As presented in the first section about ferromagnetic materials, the beads have a tendancy to attract each other in the direction of the applied field. Therefore they create chains and clusters with a major axis along the orientation of the field. During the sedimentation, these clustered structures will lay on top of each other, creating holes decreasing the compactness, as one can see in appendix C.
Our results also suggest that the compactness may reach a plateau for high values of magnetic fields, unfortunately we cannot reach these values according to our earlier remark. Nevertheless, this plateau seems to be a reasonable thought since for high values of forcing fields the structure is comparable to a brittable solid made of beads that will sediment in a few blocks, these blocks being the limit of structure reachable in our experiment. An interesting idea would be to vary the width of our cell since it seems to be the geometrical constraint for the maximum field limit.
The red line in fig. (6) corresponds to a measurement of the compactnes based on Voronoï diagrams. The Voronoï diagrams for the final structure will be presented after. The compactness of the final structure can already be defined as the inverse of the mean value of the Voronoï area of the particles forming structure. This new definition of compactness is then normalized using the area of one bead (compactness of 1 if the volume occupied is only equal to the area of the beads):

$$C_{Voronoi} = \frac{\pi a^2}{\langle area_{Voronoi} \rangle} \tag{4}$$

The resulting plot for this new definition follows exactly the same tendancy with an offset. This offset is certainly due to the inexistance of Voronoï data on the border of our structure. To conclude, these two definitions of compactness reveal that the structure is looser when we increase the forcing magnetic field, *i.e.* when we increase the attractive interactions between the beads.

Aspect ratio. In order to go deeper in the geometrical aspect of the final structure, we investigate now its aspect ratio. The aspect ratio is a direct consequence of the detection of what is called the "bounding box" of the structure, as shown in fig. (7b). In the same way as the convex hull of a points assembly, the bounding box is the smallest rectangle that contain all of our beads (*i.e.* a convex hull with only four vertices and right angles). The bounding box is easily computed for all of our structures and leads us to the definition of the aspect ratio:

$$A = \frac{height}{width} \text{ with the height and width of the bounding box} \tag{5}$$

The resulting plot for the computed aspect ratio is plotted in blue in fig. (8a). Firstly, we observe in a first region below $B = 2$ mT that the aspect ratio increases with the magnetic field. This may be attributed, as we said earlier, with the tendancy of the beads to attract each other into clusters made of chains aligned with the horizontally applied magnetic field. When sedimenting, these clusters lay on top of each other to form a final structure made of layers, creating a higher structure. For magnetic field above 2 mT, the aspect ratio tends to be slightly decreasing and seems to reach a plateau, certainly about the initial aspect ratio of ≈ 0.6 (ratio before the sedimentation). Unfortunately, there again, we cannot reach the high values of field due to the experimental limit described before. This decrease may reveal a different settling behaviour, where particles tend to fall in blocks rather than chains at stronger fields.
Secondly, we also plotted in fig. (8a) an indirect computation of the aspect ratio in red. This indirect computation is found via the compactness and defined as follows:

$$A_{compactness} = \frac{N\pi a^2}{Cwidth^2} \tag{6}$$

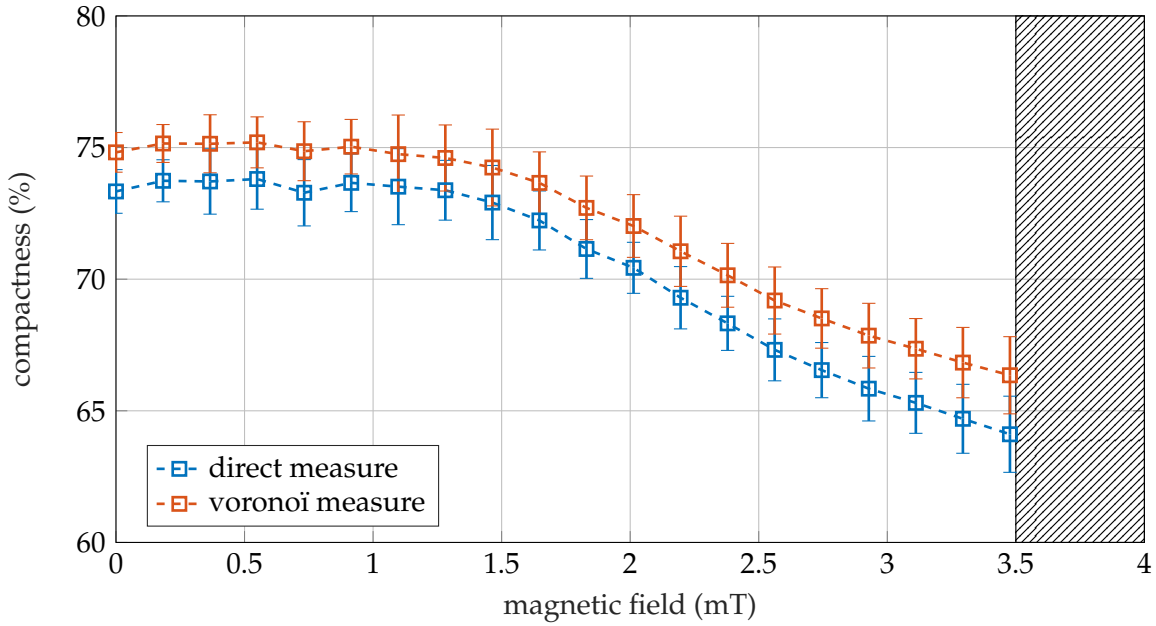

Figure 6: Compactness of the final strucutre for different values of forcing field. The blue line corresponds to the direct computation of the compactness, and the red line corresponds to a Voronoï measurement of the compactness. The two lines have the same tendancy to decrease with the increase of the field. The upper limit for the magnetic field is an experimental constraint for which the beads do not longer sediment. The error bar correspond to statistical errors on about 100 experiments for each value.

with N the number of beads, C the compactness and the width of the bounding box. This new definition consider that the final structure is a rectangle of area $width \times height$ that is equal, by definition of the compactness, to $N\pi a^2/C$. This control measurement of the aspect ratio follows the tendancy of the direct measurement. Nevertheless, a slight discrepancy exists for low values of field (below 2 mT) which corresponds to the existence of an avalanche angle in the structure. The avalanche angle is a classical granular parameter shown in fig. (7b) that represents the angle of the structure with the horizontal. Due to this angle the stucture is in reality higher than a rectangle of the same compactness. The automatic computation of the avalanche angle is given in fig. (8b), but it is computed only for small values of the external field since for higher values it is impossible to properly define an avalanche angle (one can refer to images in appendix B to be convinced). The avalanche angle reflects the friction coefficient of the granular media [13] through a Coulomb's law, and we will certainly define an effective friction coefficient in our medium tunable by the particle/particle interactions.

Application of Voronoï diagram. We have defined the Voronoï diagrams in the first section of this report and quickly used it to define the compactness. These diagrams carry more information in particular in the statistics of areas. Fig. (9) shows some examples of Voronoï diagrams obtained for the final structure for different external fields. Here again, the blue regions correspond to the smallest areas and the yellow ones correspond to the largest areas.
Fig. (10) shows the PDF of Voronoï areas for different values of amplitude of magnetic field. Before all, we deleted the regions with areas ranging from 0 mm^2 to 0.19 mm^2, this value corresponding to the area of one bead and a region of influence, cannot be less than the area of one bead. In fact these values correspond to small errors in the precise position of detected particle centers. The vertical dotted line in fig. (10) represents the value of 0.22 mm^2 representing the minimum physical value for

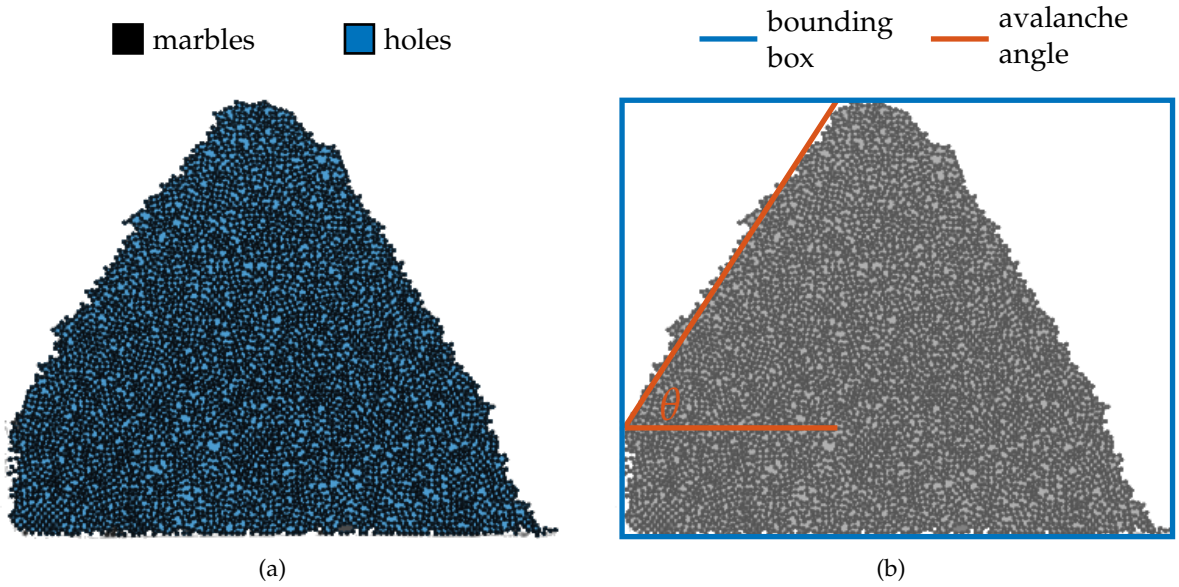

(a) (b)

Figure 7: Presentation of the different image analysis tools used for the granular study of the final sedimented structure. Fig. (7a) represents the different regions found in the final sedimented structure used to cpmpute the compactness. Between the beads (in black) we find the holes of the structure represented in blue, both regions form what we call the filled region. Fig. (7b) represents the geometrical tools to analyse the final structure. In blue is represented the bounding box of the structure, while the red lines represent the avalanche angle, *i.e.* the angle made by the border of the structure with the horizontal.

the area of Voronoï cells in the cristallized case, *i.e.* the area of the hexagon circumscribed to a circle shown in fig. (11) and of area $\mathcal{A}_{\text{hexagon}} = 2\sqrt{3}a^2$.
We can see that the most probable value of Voronoï areas increases with the magnetic field starting at a value close to the compact hexagonal cristal at small fields, up to ≈ 0.24 mm^2 for the highest. This is in agreement with the fact that the structure is loser when B increases. Secondly, the PDFs of the Voronoï areas are flatten as the applied field increases, the areas then reach higher values. This is the direct consequence of the clusters formation with the field. As we said before, the clusters will lay on top of each other creating a stable structure with big holes. These holes, or voids in this case can be seen in fig. (9c) and are a major cause of the decrease in compactness. Finally, we can see that the PDFs are quite alike for field values below 2 mT, and this observation comfort us in the idea that a new regime of sedimentation appears for field values higher than this limit, with a different behaviour.

Energy balance. The last point we have looked at in the analysis of the final sedimented structure concerns its energy. In the absence of magnetic field, a structure with a finite avalanche angle (fig. (9a) for instance) is sustained in a granular medium by the friction between grains, and by the lateral confinement, which both prevent the collapse of the stack. Here we argue that at large values of the magnetic field a balance is established between the magnetic energy of interaction between particles and the gravitational potential energy, allowing to sustain taller structures. To verify this point we propose to apply a simple energy balance to the structure. Since for small values of field the structure touches the borders of the cell we propose to work only on "independent" structures, *i.e.* for high values of field. If we consider that the only energies taking place here are the potential energy and

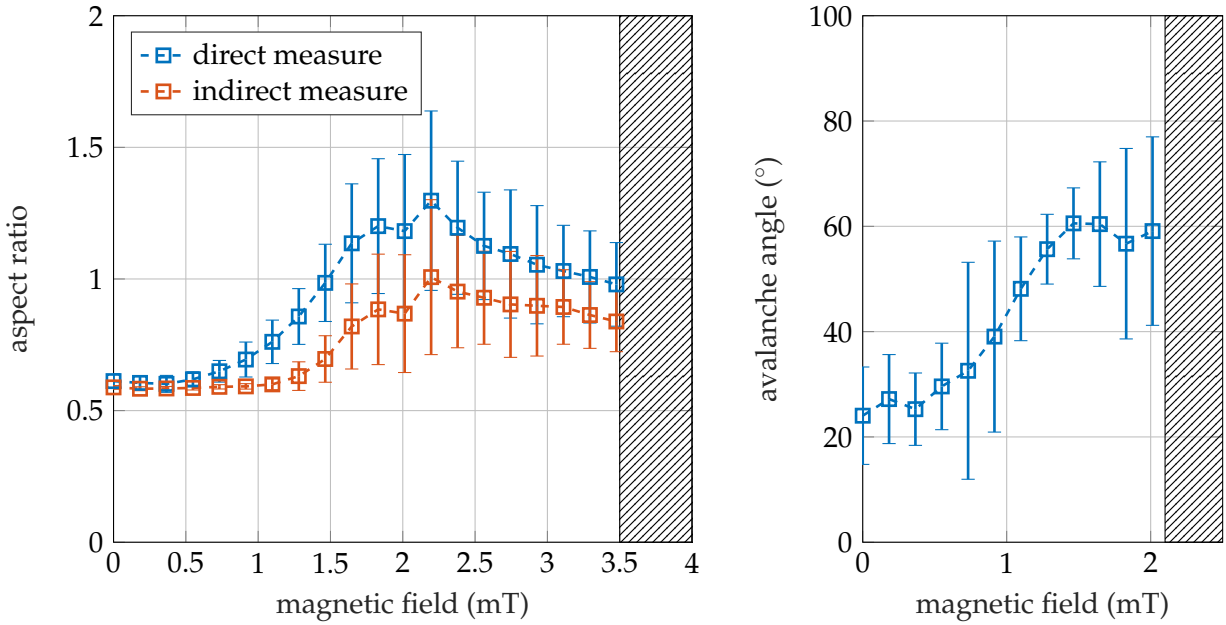

(a) (b)

Figure 8: Geometrical aspects of the final structure. Fig. (8a) shows the aspect ratio over different magnetic fields. We notice that the ratio increases until reaching a maximal value around 2 mT and then decreases, highlighting the existence of different regimes of sedimentation. The red line corresponds to a control computation of the ratio using the compactness. Fig. (8b) represents the avalanche angle of the final structure at the origin of the discrepencies between the two lines in fig. (8a). The avalanche angle is defined only for small values of field.

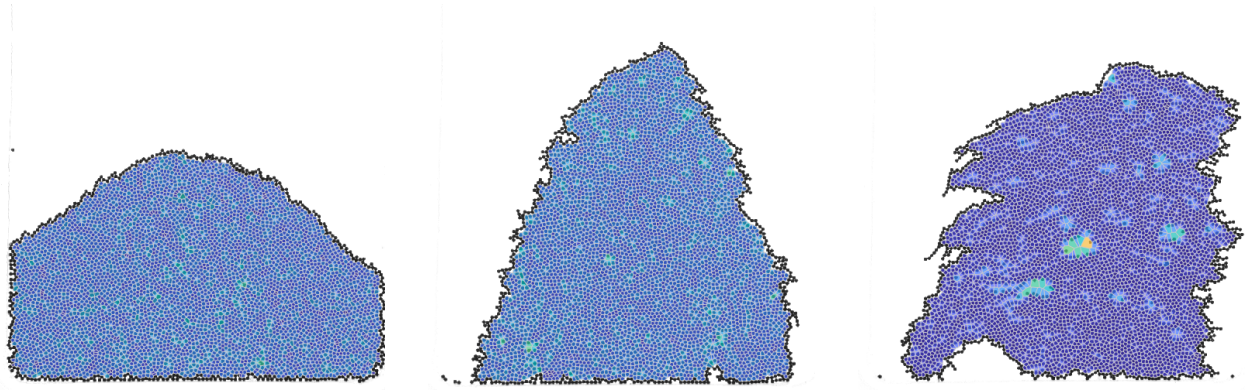

(a) $B = 0$ mT (b) $B = 1.83$ mT (c) $B = 3.66$ mT

Figure 9: Voronoï diagrams for different values of the magnetic field. We clearly notice that with high values of B, the structure is composed of large voids represented in yellow.

energy of interactions between beads (eq. 2) (in particular we neglect here the role of friction between grains) we end up with the following equality:

$$m\sum_{i=1}^{N} gy_i = \frac{\mu_0}{4\pi}\left(\frac{4}{3}\pi a^3 \chi B\right)^2 \frac{1}{2}\sum_{i,j=1}^{N}\left[\frac{1}{r_{ij}^3} - 3\frac{(x_j - x_i)^2}{r_{ij}^5}\right] \tag{7}$$

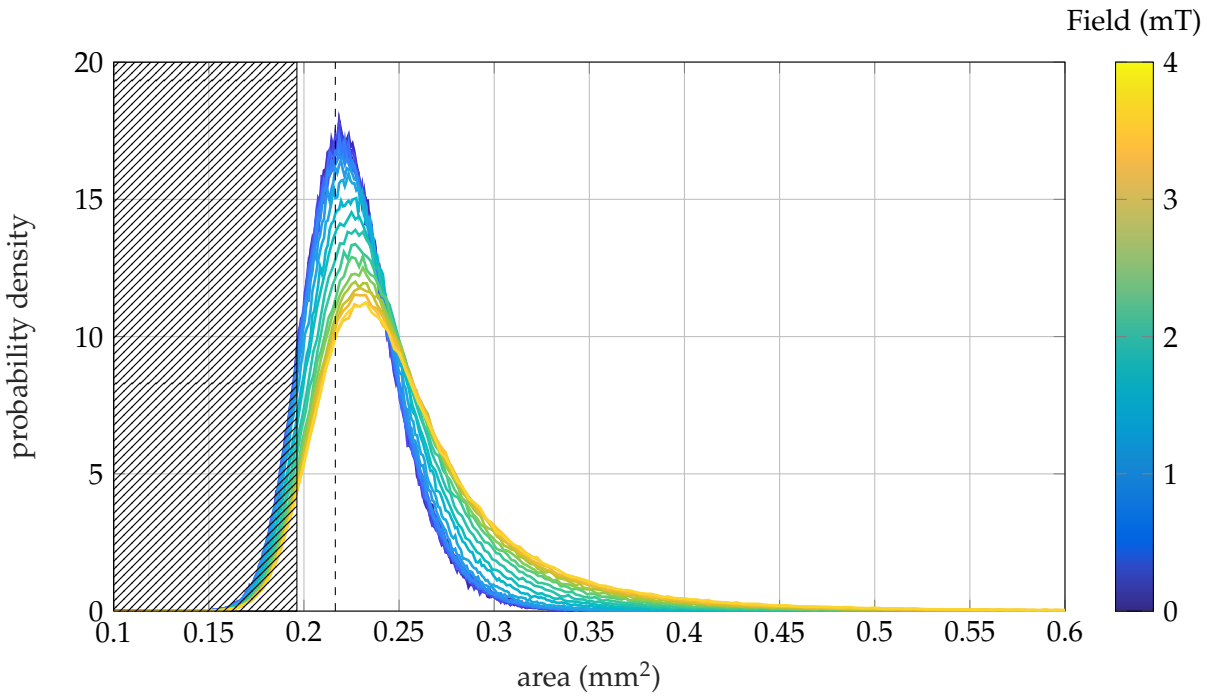

Figure 10: Probability Distribution Function of the areas of the Voronoï diagrams for all values of forcing field. The area of a bead gives us the lowest border of the graph, while the physical limit of a crystallized structure is plotted in dashed line. We clearly notice that for values of field lower than 2 mT the PDF are quite the same, while for higher values the areas tend to spread over highest values, this is the direct consequence of the apparition of voids in the structure.

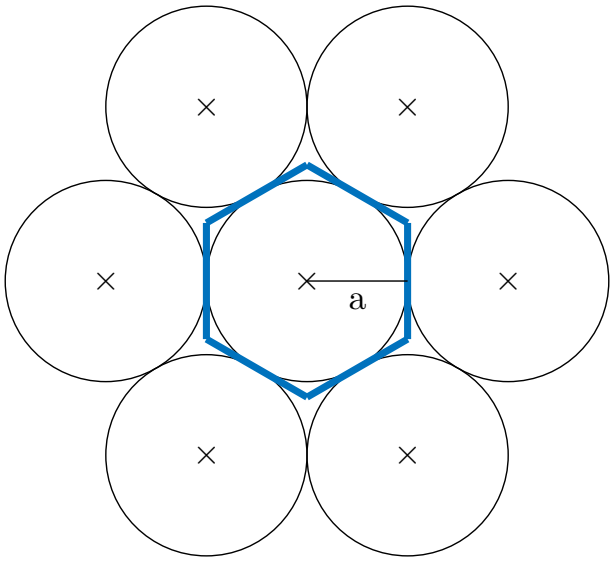

Figure 11: Representation of a cristallized state of final beads structure. The blue hexagon represents the Voronoï region of the midle bead, this hexagon is the physical minimum limit for the Voronoï diagram. The area of the hexagon circumscribed to a circle of radius a is given by $\mathcal{A}_{\text{hexagon}} = 2\sqrt{3}a^2$.

To compute the different terms of the energy balance, we identified each bead center over all of our data and computed their height and pair interaction terms. The result is plotted in fig. (12), we consider here the potential and interaction energies, respectively the left and right terms in the energy balance (1).

Our results show on one hand that the magnetic energy naturally increases with the field while on the other hand the potential energy remains constant over the different magnetic fields. These evolutions lead us to the decreasing ratio of energies plotted in fig. (12b). While the value of this ratio is of the order of magnitude of one what supports the scenario of a balance between magnetic and potential energies, we lack some explanation to explain the decrease. To sum up, the simple energy balance that we consider is a good approximation to explain the magnetically stabilized structure, but we still lack some corrections. To have a ratio of one, we would expect a decreasing potential energy. We certainly lack a better modelling of the granular medium combined to the magnetization to fully apprehend the structure. This modelization will be the subject of future investigation.

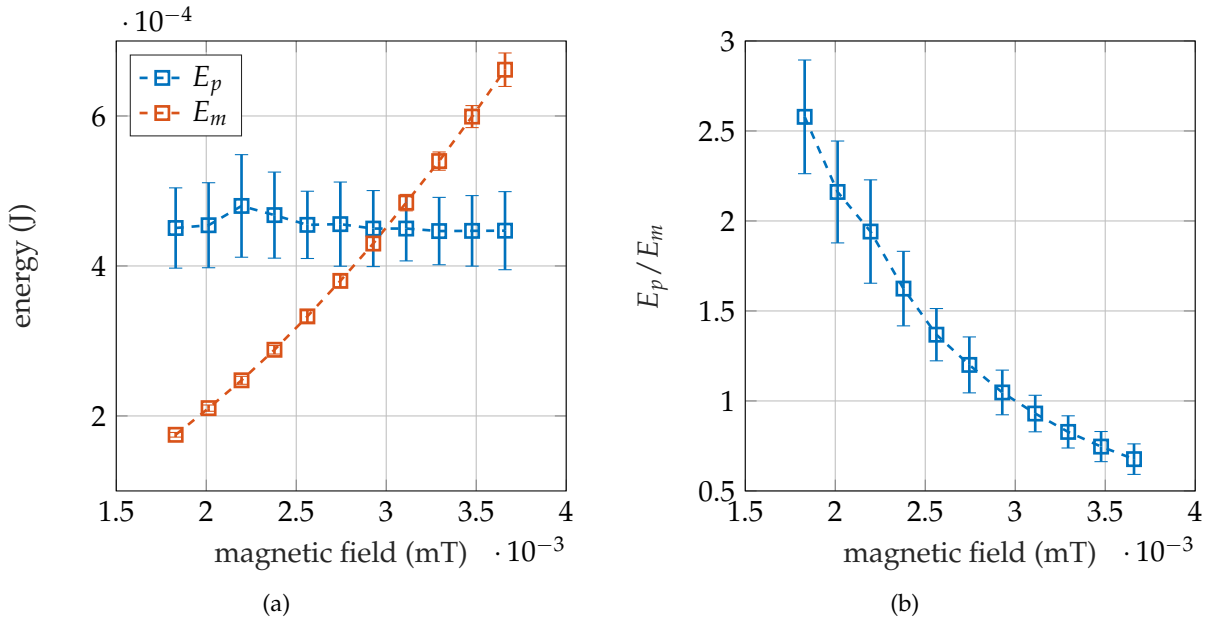

(a) (b)

Figure 12: Representation of the two different energies considered in our work. On the first plot one can see that the electromagnetic energy E_m naturally increases with the magnetic field while the potential energy E_p is constant. The ratio of the two different energies leads to the second graph for which one can see that the energy balance is quite correct but we still lack some explanation to explain the slight decrease of the ratio E_p / E_m with increasing B_0.

2 Dynamic study: clusters sedimentation

In the previous section we detailed the final sedimented structure of the beads and concluded over an amount of quantities imposed by the mechanism of sedimentation. This mechanism is changed by the magnetically tuned interactions and is the cause of a large panel of different topologies, such as it is presented in appendix C. Here we discuss the dynamics of the sedimentation, and how this sedimentation is affected by the forcing magnetic field.

Formation of clusters. As we told before in this report, because of their ferromagnetic interactions, the beads tend to create chains along the magnetic field as shown in fig. (13a). Because of the high density of particles in our case, the beads are not arranged in simple chains, but often tend to form larger clusters as shown in fig. (13b). We made a few videos (see appendix D) for different values of forcing magnetic field showing the different types of sedimenting mechanisms. To show how important the clusters are in this process, we propose to look at the instantaneous number of clusters at each time for different values of field. The maximal number of clusters gives an idea of the stability

of the sedimenting structure, this number is plotted in fig. (14a). One can clearly see that by increasing the interactions between the beads, the number of clusters drops until reaching approximately the symbolic value of one. In other words, for a limit value of field equals to approximately 2 mT, the sedimentation mechanism is no longer in terms of beads or small clusters of beads, but the fall of one large cluster, more or less deformable.

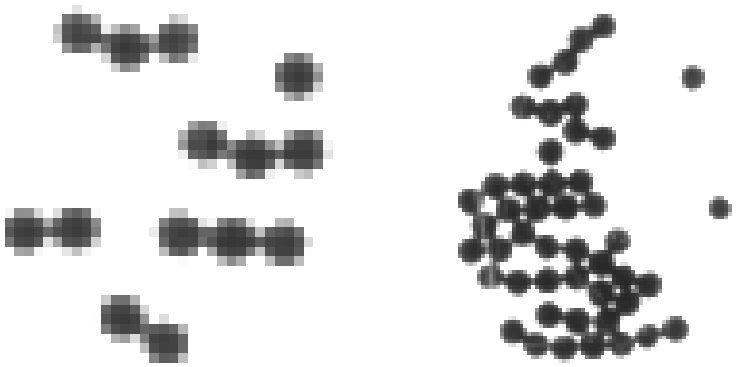

(a) $B = 0$ mT (b) $B = 1.83$ mT

Figure 13: Typical formation of beads under a forcing magnetic field. Due to the interactions the beads tend to form chains aligned along the field, but due to the high density of beads the chains are glued and form biggest clusters.

Biggest stable cluster. We look now at the size of the biggest cluster. This will give us an idea of the biggest stable clusters reachable for a given value of the magnetic field. The size of a cluster is given in terms of number of beads that composes it, and is plotted in fig. (14). For small fields, as the number of clusters decreases, their sizes increases. Then the number of clusters for high values of field varies around one, and that nearly all the beads ($\approx$ 5000 beads) are contained in only a few number of clusters. Secondly, we notice that the maximal size of cluster is not reached for the highest values of field, but around $1 - 2$ mT. This can be understood by watching the different sedimentation videos in appendix D: for high values of field the sedimenting structure composed of a large number of particles is "solid" and the resistance of the fluid is high on it. Because of the hydrodynamics flowing against this strucure, the clusters tend to crush into smaller pieces to finally sediment. For smallest values of field (around 2 mT here), we notice that the sedimenting structure is far more deformable and tends to follow the englobing hydrodynamics and falls in one piece.

"Elastic" cluster. To apprehend this question of deformability of the biggest cluster we propose to quickly look at the final stage of the sedimentation for $B = 1.83$ mT, for which the sedimentation is of only one big cluster that deforms itself when touhcing the bottom of the cell. We notice by plotting the aspect ratio of the structure when it touches the bottom of the cell that the structure is going to deform itself as one can see in fig. (15). This graph is taken from the full video findable on bit.ly/final_ar_steel_250um_18G.

3 Back to compactness

Finally, we want to come back to the compactness of the final structure and connect it to the settling dynamics. We told in the first section that this compacity is the result of different clusters sedimenting, creating holes that make the compactness drop. To verify this, we propose to plot in different colors the clusters that sedimented to finally form this final sedimented structure. To do so we track the different clusters in our videos until they reach the bottom. The color figures for two different

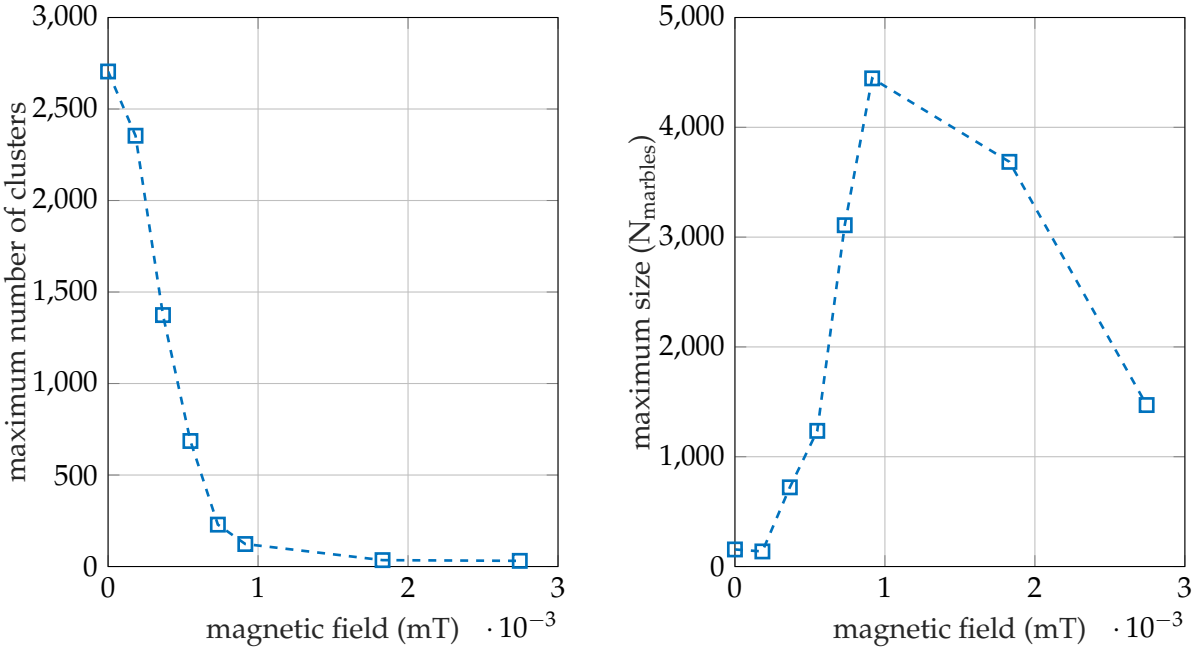

(a) (b)

Figure 14: Presentation of the evolution of clusters when changing the intensity of the magnetic field. The first graph represents the maximal number of clusters created inside the cell for a given magnetic field. When this maximal number of clusters is found, we have access to the biggest stable cluster for a given magnetic field, its size in terms of beads is given in the second graph.

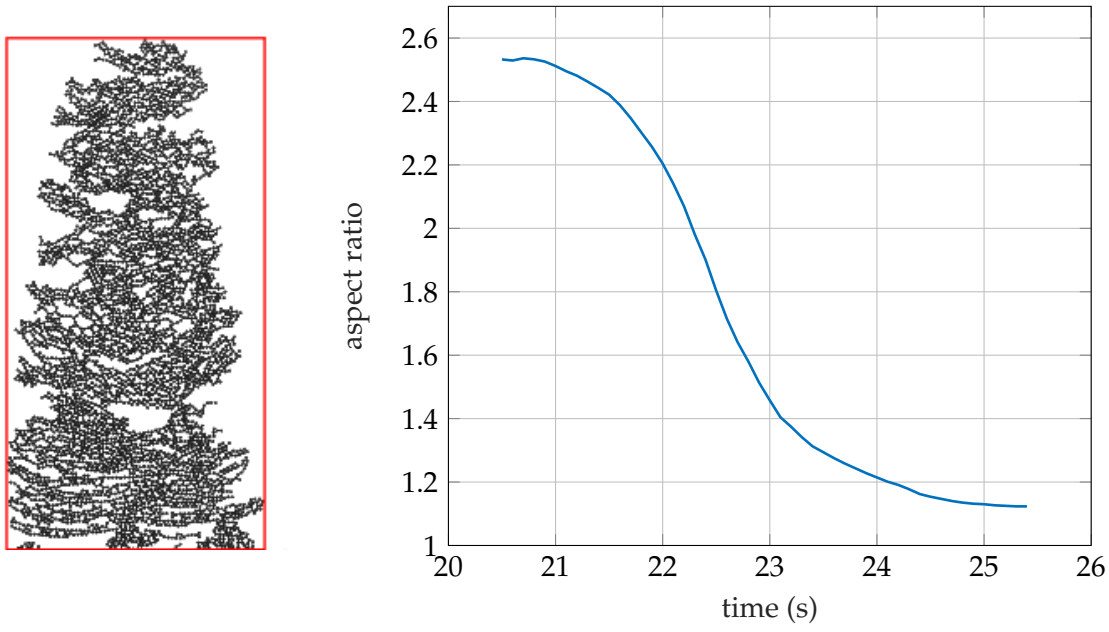

(a) (b)

Figure 15: Evolution of the aspect ratio of the sedimenting structure when it reaches the bottom of the cell. The aspect ratio is here again defined by using the bounding box (shown in red) and decrease by following the blue line. The value of field is 1.83 mT.

values of field are shown in fig. (16). Firstly, for a medium value of field (1.83 mT) we notice that the structure is composed only of two clusters, one containing nearly all the beads, this is the deformable cluster we talked about. Secondly, for high value of field (2.75 mT) we notice that the number of clusters is more important, but most importantly we notice that on one hand the clusters have proper holes, fixed by the solidity of the cluster, but on the other hand we also notice holes induced by the stacking between two different clusters that also make the compactness drop.

(a) $B = 1.83$ mT (b) $B = 2.75$ mT

Figure 16: Final formations of the sedimented structure for two values of magnetic field. The different colors correspond to different clusters that sedimented to finally create this stable structure.

To conclude over the clusters dynamics, it is clear that they are at the heart of the mechanism responsible for the final compactness, although a full modelling is still required to accout for large variety of parameters of the clusters need to be taken into account such as the "solidity", size, aspect ratio, ... and their impact on the final structure.

III Food for thought

In this section we would like to give a taste of two different questions that were raised when we performed the experiments. These studies are far from giving results but they will play a key role in the future understanding of all the key mechanisms acting here.

1 Influence of initial state

The first thing that we want to explore is the influence of the initial state on the sedimentation process. At the moment our protocol starts from a sedimented structure that is flipped again under the forcing of an external magnetic field. This structure has its proper compactness, aspect ratio, etc. To bypass this starting limitation we propose to start the sedimentation from a homogeneous concentration of beads. To do so we propose a new protocol for our experiment:

homogeneization: when we flip N times the cell until reaching a homogeneous state,

sedimentation: when we wait for the sedimentation of the homogeneous state with our without forcing field.

The homogeneization part is done by flipping again and again the cell, like shaking the pulp of a bottle, until reaching a homogeneous state for the suspended beads. To control that our state is rightfully homogeneous we take snapshots of the cell at each flipping and verify that we reach the wanted state. For each picture we control the error on the homogenity by computing the ratio of the standard deviation of the concentration over its mean value. We propose that our homogenous state is reached when we have a stabilized error of less than five percent, as it is shown in fig. (17a). The homogeneous state is reached after 30 flippings, and can be seen in fig. (18). To control our homogeneous state, we also propose to plot the pair-distribution function g defined in [14] as:

$$g(r) = \left\langle \frac{A}{N^2} \sum_{i=1}^{N} \sum_{j \neq i=1}^{N} \delta(r - r_{ij}) \right\rangle, \tag{8}$$

with A the area of research and N the number of beads in this area. This function gives us the probability to find a bead in a circle of radius r centered on one of the bead. The function for our experiment is shown in fig. (17b). We see that the global shape of our function is the same as the one of a perfectly random distribution, with a peak found at a $r = 2a$, [14].
To sum up, our protocol of homogeneization of our beads suspension is correct and can be used to study our experiment without any constraint of the initial state. This study is planned for future works, but some videos have already been made such as: bit.ly/homogeneous_steel_250um_36G.

2 Hydrodynamics of Hele-Shaw flow

Finally, we noticed that the flow of quasi-2D spheres in a Hele-Shaw cell is not well documented. We found only a few references dealing with the subject (such as [15] or [16]) and giving us a few basic elements to understand the flows we are dealing with in our experiment. We noticed that the sedimentation of our clusters is controlled by the width of our cell, creating a lot of recirculation flows inside the cell. For the moment we lack observations of the flow around the beads and the clusters. In order to fully apprehend the hydrodynamics in our experiment, we have adden tracers inside the fluid. To do so we use 50 µm polyethylene tracers with a density slightly less than the glycerol/water mix. Then, we perform Particle Tracking Velocimetry on the tracers to access the hydrodynamics.
This study is still at its early stage, but we plan to investigate the following regimes:

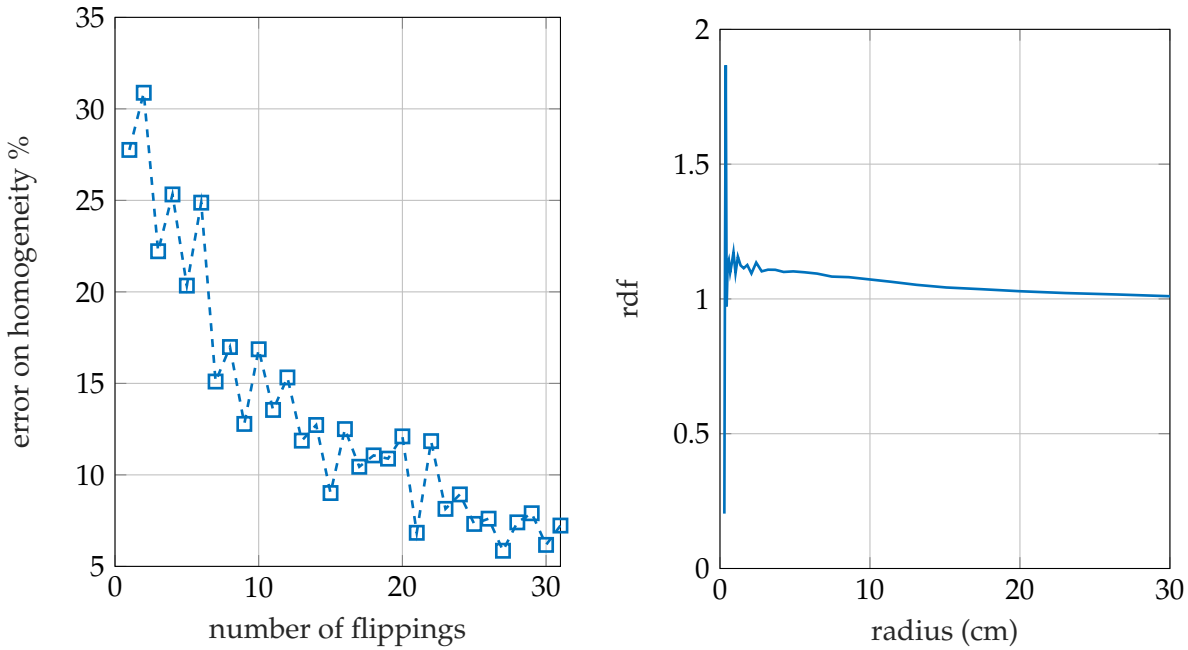

(a) (b)

Figure 17: Control graphs to test the accuracy of our homogeneous state. The error in homogeneity is given by the ratio of the standard deviation over the mean value of concentration of our suspension. The other plot is the pair-distribution function that represent the probability to find an other bead in a given circle of radius r.

Re	$O(0.1)$	$O(1)$	$O(10)$
beads	steel of 500 µm diameter	glass of 500 µm diameter	glass of 500 µm diameter
liquid	water/glycerol mix 77%	water/glycerol mix 47%	water

For each value of the Reynolds number we propose to study four values of the concentration in beads: 0.5%, 1.5%, 4%, 10%.
A close up of the tracers around the beads is shown in fig. (19), and a video using the tracers is found by following this link: `bit.ly/sedimentation_tracers_steel_250um`.

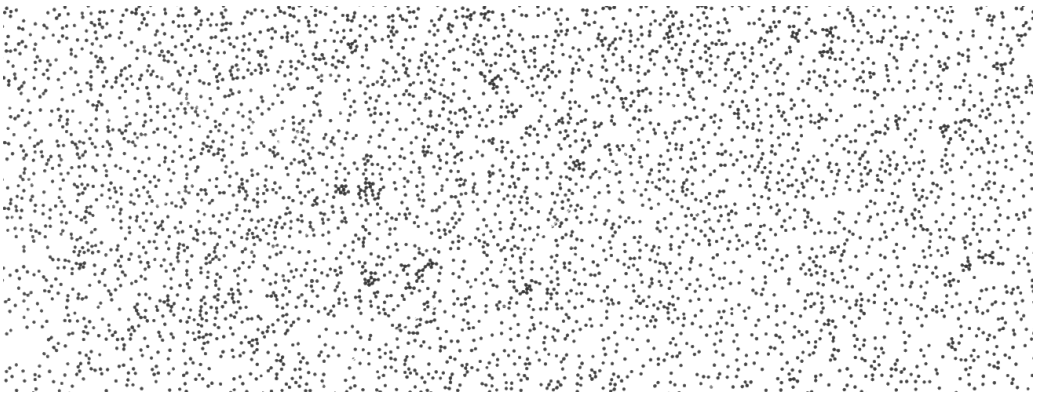

Figure 18: Homogeneous state, reached after 30 flipping of the cell.

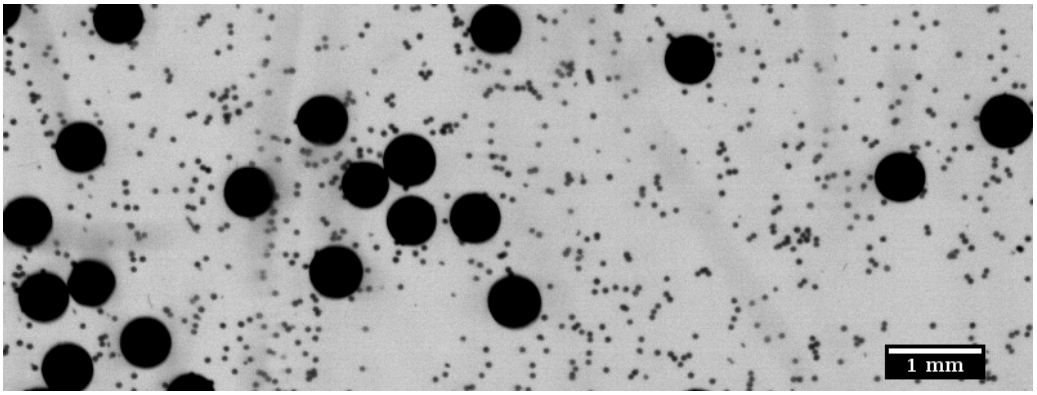

Figure 19: Close up of the tracers of 50 μm diameter used to track the hydrodynamics of the Hele-Shaw flow around the beads using a PTV analysis.

Conclusion

Our experiment was designed to explore the suspensions of magnetic materials under the influence of an external magnetic field, but we quickly found that our quasi-2D state in a Hele-Shaw cell is, on his own, very promising. A large panel of studies need to be performed in order to fully apprehend all the mechanisms involved in the sedimentation.
We firstly performed a more granular-type study to describe the sedimented final structure. We clearly notice that the influence of the magnetic field, *i.e.* of the interactions between beads, are visible and mesurable in terms of compactness, aspect ratio and avalanche angle of the final structure. We also noticed that it might exists a value of field (around 2 mT) for which the sedimenting mechanisms are slightly different. In fact these differences are noticed when we perfomed the analysis on the dynamics of clusters sedimentation. The clusters are formed by the mutual attractions of the beads, but they react differently with the value of the field with a continuous transition from an actual granular expansion at low fields to an assembly of deformable porous clusters at modest field and eventually solid (and brittable) porous clusters at large field. Indeed for high values of field the sedimenting clusters are no longer granular media but react more like porous solid media. We still need to conduct further analysis for these values of field but also for low values for which the clusters are smaller but clearly have an impact as the granular analysis reveals. Moreover, we conducted a reduced energy balance to apprehend the mechanisms involved inside the final structure, but for the moment we still lack a complete modelisation of the processes, that will be done in the future work on this experiment. Finally, we also propose to study the influence of the initial state by imposing a homogeneity that seems to be reached in our latest viedos. We also noticed the lack in litterature of some basic description of the hyrodynamics inside a Hele-Shaw cell around a sedimenting sphere, we propose to explore this subject by using tracers.

Appendix A Bead size distribution

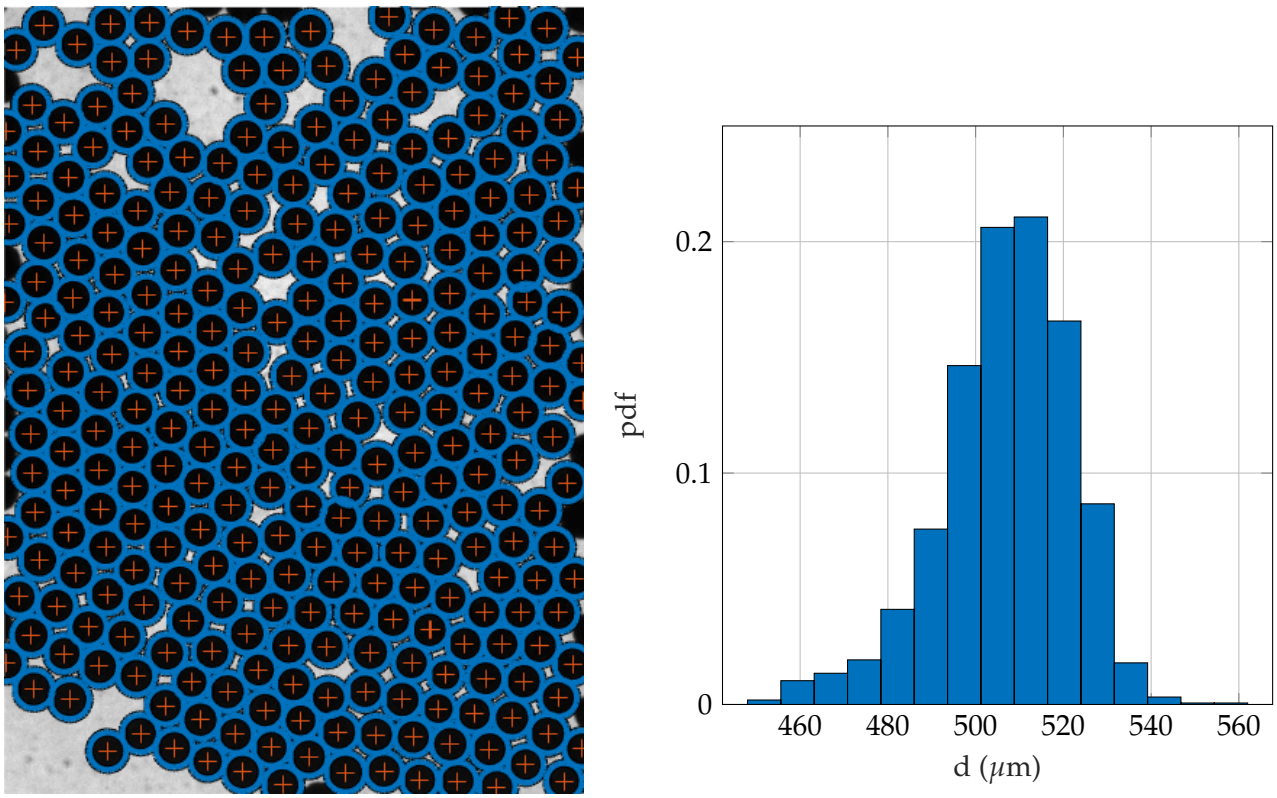

(a) (b) pdf

Figure 20: Principle of the size measurement of our beads.

To measure the size distribution of our beads we used a "Makroscope" in order to have a picture of our beads sufficiently zoomed to perform a circle detection. The measurement is performed on about 1400 beads and we obtain a circle detection such as the one shown in fig. (20a). Therefore, all the results are computed in a single PDF shown in fig. (20b). We can conclude that our beads are monodisperse spheres of approximately 500 µm diameter.

Appendix B Magnetic susceptibility of the beads

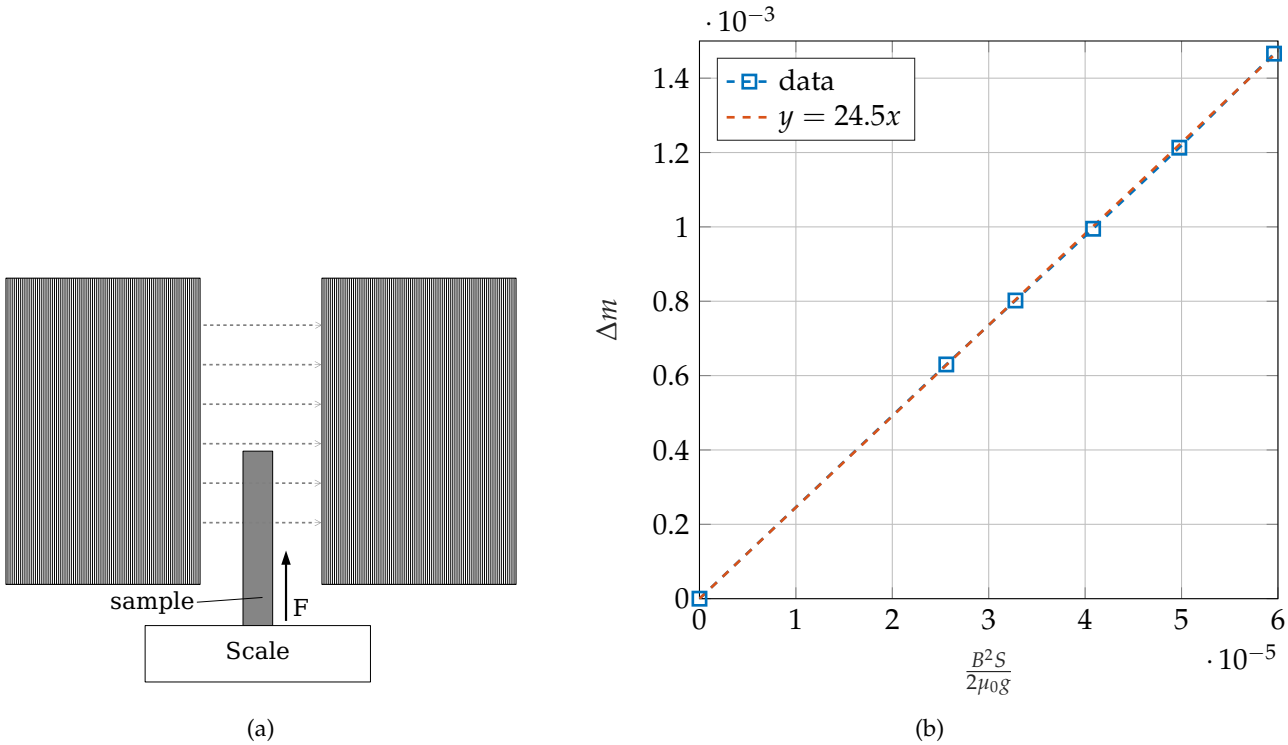

(a) (b)

Figure 21: Presentation of the Gouy scale used to measure the magnetic susceptibility of a sample placed between two coils. The experimental data are given in fig. (21b), the susceptibility of the sample is given by the slope.

The experimental setup that we used to measure the magnetic susceptibility of our ferromagnetic beads is a Gouy scale [17] presented in fig. (21a). The idea is to put a part of the sample between two coils creating a strong magnetic field, this will create a force acting on the sample, creating an effective difference of mass. The force is given by:

$$F = \frac{1}{2}\mu_0 H^2 S\,(\chi - \chi_{air}) \tag{9}$$

with H the forcing field, χ_{air} the susceptibility of air, χ the measured susceptibility and S the cross-section of sample in the direction of the field. Since the magnectic susceptibility of air is negligeable, we can rewrite this equation in terms of effective loss of mass:

$$g\Delta m = \frac{1}{2\mu_0} B^2 \chi S \Leftrightarrow \Delta m = \frac{B^2 S}{2\mu_0 g} \times \chi \tag{10}$$

The magnetic susceptibility of the medium is found by plotting Δm function of $\frac{B^2S}{2\mu_0 g}$, the plot is shown in fig. (21b). We found $\chi = 24.5$, but this would be the case for a continuous medium. Since we work here with a granular medium we need to divide this result by the compacity of the sample ($C = 0.56$ in our case).
We can conclude the the magnetic susceptibility of our beads is $\chi = 44$.

Appendix C Final sedimentation pattern

(a) $B = 0$ mT (b) $B = 0.18$ mT (c) $B = 0.36$ mT (d) $B = 0.55$ mT (e) $B = 0.73$ mT

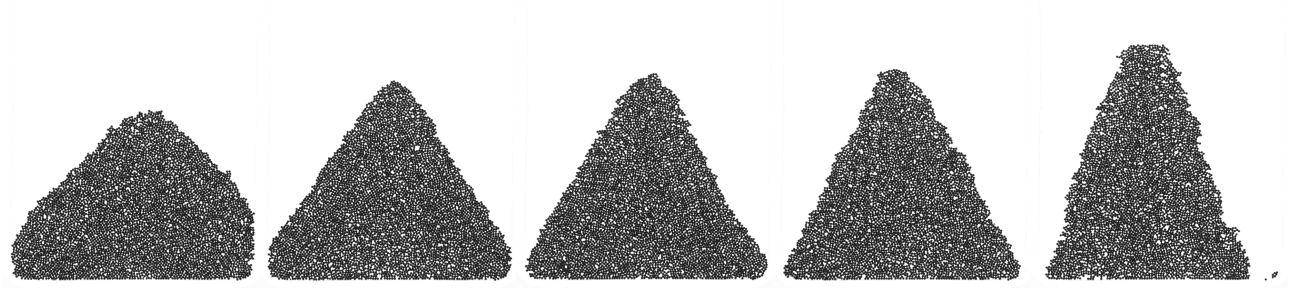

(f) $B = 0.92$ mT (g) $B = 1.10$ mT (h) $B = 1.28$ mT (i) $B = 1.46$ mT (j) $B = 1.65$ mT

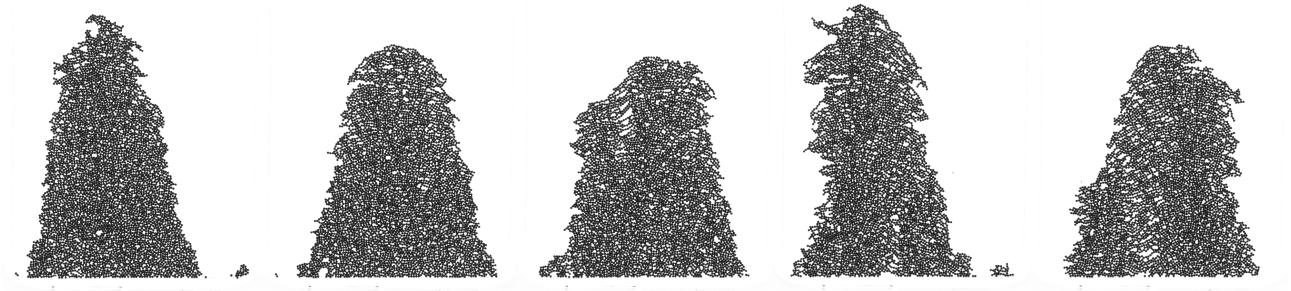

(k) $B = 1.83$ mT (l) $B = 2.01$ mT (m) $B = 2.20$ mT (n) $B = 2.38$ mT (o) $B = 2.56$ mT

(p) $B = 2.75$ mT (q) $B = 2.93$ mT (r) $B = 3.11$ mT (s) $B = 3.29$ mT (t) $B = 3.48$ mT

(u) $B = 3.66$ mT

Appendix D Different videos

The videos of sedimentation presented in the second section can be seen by following these links:

$B = 0$ mT	bit.ly/sediment_steel_250um_0G
$B = 0.18$ mT	bit.ly/sediment_steel_250um_1G
$B = 0.36$ mT	bit.ly/sediment_steel_250um_3G
$B = 0.55$ mT	bit.ly/sediment_steel_250um_5G
$B = 0.92$ mT	bit.ly/sediment_steel_250um_9G
$B = 1.83$ mT	bit.ly/sediment_steel_250um_19G
$B = 2.75$ mT	bit.ly/sediment_steel_250um_27G

Video of the aspect ratio of the deformable cluster: bit.ly/final_ar_steel_250um_18G

Video of the sedimentation starting from an homogenous state and under a magnetic field: bit.ly/homogeneous_steel_250um_36G

Video of the use of tracers inside the Hele-Shaw cell: bit.ly/sedimentation_tracers_steel_250um

Bibliography

[1] R. Miao and S. Saxena, "A theory for agglomeration and sedimentation of ferromagnetic particles suspended in a hydrocarbon liquid and exposed to a magnetic field," *Powder Technology*, vol. 86, pp. 187–194, feb 1996.

[2] Z. Yildiz, T. Abbasov, and A. Sarimeseli, "Effect of the magnetization properties of the granular beds and the operating parameters on the removal ferrous particles from the waters by using magnetic filter," *Particulate Science and Technology*, vol. 31, pp. 109–113, mar 2013.

[3] M. Cox, D. Wang, J. Barés, and R. P. Behringer, "Self-organized magnetic particles to tune the mechanical behavior of a granular system," *EPL (Europhysics Letters)*, vol. 115, p. 64003, sep 2016.

[4] A. Snezhko, I. S. Aranson, and W.-K. Kwok, "Structure formation in electromagnetically driven granular media," *Physical Review Letters*, vol. 94, mar 2005.

[5] A. Porath-Furedi and P. Yanai, "Phenomenon of migration and sedimentation of erythrocytes induced by magnetic fields.," *Journal of Histochemistry & Cytochemistry*, vol. 27, pp. 371–374, jan 1979.

[6] M. Gusenbauer, A. Kovacs, F. Reichel, L. Exl, S. Bance, H. Özelt, and T. Schrefl, "Self-organizing magnetic beads for biomedical applications," *Journal of Magnetism and Magnetic Materials*, vol. 324, pp. 977–982, mar 2012.

[7] N. A. Spaldin, *Magnetic Materials*. Cambridge University Press, 2009.

[8] B. F. Edwards and J. M. Edwards, "Dynamical interactions between two uniformly magnetized spheres," *European Journal of Physics*, vol. 38, no. 1, 2017.

[9] J.-S. Ferenc and Z. Néda, "On the size distribution of poisson voronoi cells," *Physica A: Statistical Mechanics and its Applications*, vol. 385, pp. 518–526, nov 2007.

[10] R. Aleixo, S. Soares-Frazão, and Y. Zech, "Velocity-field measurements in a dam-break flow using a PTV voronoï imaging technique," *Experiments in Fluids*, vol. 50, pp. 1633–1649, dec 2010.

[11] Y. Zhang, Y. Wang, B. Yang, and W. He, "A particle tracking velocimetry algorithm based on the voronoi diagram," *Measurement Science and Technology*, vol. 26, p. 075302, jun 2015.

[12] H. Kausch, D. Fesko, and N. Tschoegl, "The random packing of circles in a plane," *Journal of Colloid and Interface Science*, vol. 37, pp. 603–611, nov 1971.

[13] Y. Forterre and O. Pouliquen, "Flows of dense granular media," *Annual Review of Fluid Mechanics*, vol. 40, pp. 1–24, jan 2008.

[14] F. Rouyer, D. Lhuillier, J. Martin, and D. Salin, "Structure, density, and velocity fluctuations in quasi-two-dimensional non-brownian suspensions of spheres," *Physics of Fluids*, vol. 12, pp. 958–963, may 2000.

[15] E. Kuusela, J. M. Lahtinen, and T. Ala-Nissila, "Sedimentation dynamics of spherical particles in confined geometries," *Physical Review E*, vol. 69, jun 2004.

[16] A. Alvarez and R. Soto, "Dynamics of a suspension confined in a thin cell," *Physics of Fluids*, vol. 17, p. 093103, sep 2005.

[17] L. J. Brubacher and F. E. Stafford, "Magnetic susceptibility: A physical chemistry laboratory experiment," *Journal of Chemical Education*, vol. 39, p. 574, nov 1962.